Dissociative Photodetachment Dynamics of Solvated Iodine Cluster Anions

M. Shane Bowen,[†] Maurizio Becucci,[‡] and Robert E. Continetti*[,†]

Department of Chemistry and Biochemistry, University of California, San Diego. 9500 Gilman Drive, La Jolla, California 92093-0340, and European Laboratory for Non-Linear Spectroscopy (LENS), Polo Scientifico dell'Università, Via N. Carrara 1, 50019 Sesto Fiorentino, Firenze, Italy

Received: August 22, 2005; In Final Form: October 17, 2005

Photoelectron-photofragment coincidence spectroscopy of $I^-(CO_2)$, $I^-(NH_3)$, $I^-(H_2O)$, $I^-(C_6H_5NH_2)$, and $I^-(C_6H_5OH)$ clusters was used to study the dissociative photodetachment (DPD) dynamics at 257 nm. Photodetachment from all five clusters was observed to yield bound neutral clusters as well as the DPD products of the iodine atom and the molecular solvent. Photoelectron images and kinetic energy spectra were recorded in coincidence with both the translational energy released between dissociating neutral products and stable neutral clusters. The variation of the photoelectron angular distributions in the clusters was measured, revealing significant perturbations relative to I^- for $I^-(H_2O)$ and $I^-(C_6H_5NH_2)$. Product branching ratios for stable versus dissociative photodetachment and photodetachment to the $I(^2P_{3/2})$ and $I(^2P_{1/2})$ states are reported. The measurements reveal a dependence of the DPD dynamics on the final spin−orbit state of iodine in the cases of $I^-(C_6H_5NH_2)$ and $I^-(CO_2)$ and a threshold detachment process in $I^-(C_6H_5NH_2)$.

Introduction

Studies of solvation phenomena have been an active area of research rich with fundamental insights. The motivation of these studies is to obtain a better understanding of the microscopic interactions that govern the aggregation of matter to form bulk materials.[1,2] Probing the electronic structure of halogen atoms and ions clustered with small molecules yields insights into weak interactions such as van der Waal forces, hydrogen bonding, charge-dipole or quadrupole, and charge-induced-dipole interactions. The focus of the experiments reported here is to study the half-collision dynamics of the small halogen-molecule dimers, $I(CO_2)$, $I(NH_3)$, $I(H_2O)$, $I(C_6H_5NH_2)$, and $I(C_6H_5OH)$ when these constituents are initially configured in the equilibrium geometries of the corresponding anions. Photoelectron-photofragment coincidence (PPC) measurements probing the dissociative photodetachment (DPD) dynamics of these anionic clusters are presented. These DPD measurements provide complementary observations to previously measured photoelectron spectra, reviewed below, on $I^-(CO_2)$, $I^-(H_2O)$, and $I^-(NH_3)$ and represent the first photodetachment measurements on $I^-(C_6H_5NH_2)$ and $I^-(C_6H_5OH)$. These measurements constitute the first study of the dissociation dynamics of the neutral clusters formed by photodetachment of these anions, significantly extending previous studies of solvation phenomena in halogen− and halide−solvent clusters.

A number of experimental measurements on stepwise-solvated negative-ion clusters have been carried out using conventional and threshold photoelectron spectroscopies.[3−11] The relative ease of generating halide anion clusters with a variable number of solvent molecules makes them convenient starting systems to study mass-selected molecular aggregates.[12−17] Recently, photoelectron imaging has been used to characterize the angular distributions and electronic state branching ratios for a series of solvated iodine anions.[18] The excess charge was found to be localized on the halogen atom, and the atomic electronic transitions are replaced by bands of transitions resulting from internal excitation in the neutral clusters after photodetachment. Results from such experiments provide information about the structures of the anions and the corresponding neutrals, the vibrational modes, and the heats of formation of the cluster anions. This information has allowed generation of empirical potential energy functions describing the interactions of the cluster constituents.[11,19] None of those studies have directly monitored the dynamics of neutral clusters that dissociate upon anion photodetachment.

The predissociation dynamics of neutral clusters has also been the focus of a number of experimental and theoretical studies. This body of work, too extensive to review in detail here, has included laser-induced fluorescence studies of the excited states of neutral clusters formed in supersonic molecular beams.[20−23] In general, it has been found that the lifetimes of the excited states in clusters are shorter than the corresponding states of the isolated molecules, and evidence for mode-specific lifetimes has also been reported.[24−26] The dissociation dynamics of neutral clusters have also been studied by translational spectroscopy.[27−32] Recently, ion-imaging techniques have allowed simultaneous observation of the recoil energy and angular distributions of dissociating neutral dimers.[33,34] These studies indicate that the translational energy (E_T) distribution of the recoiling fragments typically peaks near zero and monotonically decreases with increasing E_T, consistent with unimolecular decomposition in the absence of a barrier.

A number of photodetachment measurements have been carried out on the $I^-(CO_2)$ and $I^-(H_2O)$ clusters.[15,16,18,19,35] Photoelectron spectra and high-pressure mass spectrometry (HPMS) measurements have been reported for the $I^-(NH_3)$ cluster,[36,37] and negative ion chemical ionization (NICI) and HPMS were used to study $I^-(C_6H_5NH_2)$ and $I^-(C_6H_5OH)$.[13,17] These systems exhibit two fundamentally different types of interactions. Neumark and co-workers found that bonding in

* Corresponding author. E-mail: rcontinetti@ucsd.edu.
† University of California, San Diego.
‡ European Laboratory for Non-Linear Spectroscopy.

10.1021/jp0547358 CCC: $30.25
Published on Web 12/02/2005

the $I^-(CO_2)$ cluster is governed by electrostatic charge−quadrupole and charge-induced-dipole interactions, yielding a distorted T-shaped structure with C_{2v} symmetry.[15] In contrast, the $I^-(NH_3)$ and $I^-(H_2O)$ clusters are bound by charge−dipole interactions coupled with hydrogen bonding.[16,36] The strengths of these interactions are influenced by the dipole moments of the solvent molecules ($\mu = 1.471$ D for NH_3 and 1.854 D for H_2O),[38] as well as the acidity of the solvent. These interactions are reflected in the stability of the anionic clusters: $I^-(CO_2)$ is more stable than atomic I^- by 0.19 eV;[15] $I^-(NH_3)$ is more stable by 0.29 eV;[36,37] and $I^-(H_2O)$ is more stable by 0.39 eV.[16] The HPMS and NICI measurements on $I^-(C_6H_5NH_2)$ and $I^-(C_6H_5OH)$ indicate that these two systems are more stable than I^- by 0.56 and 0.75 eV, respectively.[13,17] Since aniline ($C_6H_5NH_2$) and phenol (C_6H_5OH) both have smaller dipole moments than NH_3 or H_2O ($\mu = 1.13$ D for $C_6H_5NH_2$ and 1.224 D for C_6H_5OH),[38] hydrogen bonding and higher order effects such as charge-induced-dipole interactions with the polarizable aromatic ring evidently contribute to their enhanced stability.

In the present study, PPC spectra recorded for both stable and dissociative photodetachment of $I^-(CO_2)$, $I^-(NH_3)$, $I^-(H_2O)$, $I^-(C_6H_5NH_2)$, and $I^-(C_6H_5OH)$ anions at 257 nm are presented. This technique allows discrimination between stable photodetachment and DPD by measuring the photofragments in coincidence with the photodetached electron. The energy available for dissociation is determined by the photon energy and the photoelectron kinetic energy (eKE). The photon energy used here (4.82 eV) allowed production of both the ground, $^2P_{3/2}$, and first excited, $^2P_{1/2}$, electronic states of the iodine atom as neutral products. Due to the rapid photodetachment process, these measurements probe the half-collision dynamics of the neutral cluster constituents when they are configured in the equilibrium geometries of the anions. Following a discussion of the experimental approach, PPC measurements are presented that probe the DPD dynamics, energetics, and product branching ratios for these solvated iodide anions.

Experiment

Photoelectron-photofragment coincidence spectroscopy of solvated I^- clusters was performed using a fast-ion-beam PPC spectrometer. This spectrometer allows the measurement of both photoelectron and photofragment kinetic energies and angular distributions in coincidence. The details of the experimental apparatus have been described previously,[39−41] therefore only a review is now presented.

The cluster anions were generated using a 1 keV electron-impact ion source on a 1 kHz pulsed supersonic expansion of <5% CF_3I/Ar mixed with the solvent of interest. This source forms I^- through dissociative attachment of low-energy secondary electrons to CF_3I. Production of $I^-(CO_2)$ and $I^-(NH_3)$ clusters involved mixing the CF_3I/Ar carrier gas with CO_2 or NH_3 (6:1 for (CF_3I/Ar):CO_2 and 1:1.75 for (CF_3I/Ar):NH_3). The $I^-(H_2O)$ and $I^-(C_6H_5NH_2)$ anions were generated by bubbling the CF_3I/Ar mixture through H_2O or $C_6H_5NH_2$ at room temperature. $I^-(C_6H_5OH)$ anions were formed by passing the CF_3I/Ar mix over solid C_6H_5OH at room temperature. Following anion generation, the expansion was skimmed, accelerated to 5 keV, and then re-referenced to ground potential using a high-voltage switch.[42] The anions were mass-selected by time-of-flight (TOF) and transported into the laser interaction and detection chamber. The *m*/*z* anion of interest was then perpendicularly intersected with a ∼1.8 ps full width at half-maximum (fwhm) linearly polarized third harmonic pulse (257 nm, 4.82 eV) from a regeneratively amplified Ti:Sapphire laser (Clark CPA 2000). The laser beam was focused onto the ion packet yielding typical peak power densities of 120 MW/cm^2.

After interaction with the laser, residual anions were electrostatically deflected out of the molecular beam and the remaining neutral species impinged on a time- and position-sensitive detector. The neutral particle detector consists of a stack of three 40 mm diameter microchannel plates in front of a fast-crossed-delay-line anode. If a stable cluster was produced by photodetachment, a single particle struck the detector at the time- and position-of-arrival of the parent beam. However, if DPD occurred, two momentum-matched fragments were recorded and the photofragment masses and center-of-mass translational energy release (E_T) was calculated. In this investigation, we used a new crossed-delay-line anode that requires no blocker[40] and thus has no significant detector acceptance limitations other than ≈10 ns dead time between particles, but because of this the translational energy distributions reported here will represent $N(E_T)$, the number of events with a given E_T. These $N(E_T)$ will underestimate the true $P(E_T)$ at $E_T = 0$ as a result of the dead time in two-particle detection. The effect of the dead time is a function of the dissociation kinematics, E_T, and the experimental configuration, all of which are reasonably similar in these measurements. Comparison of one- and two-particle TOF spectra for the $I^-(CO_2)$ and $I^-(C_6H_5NH_2)$ spectra indicate that on the order of 18% of two-particle coincidence events will be lost due to the dead time in the present experiments. Calibration of the neutral particle detector was done through DPD measurements on O_4^-; the E_T resolution was found to be ∼9% $\Delta E_T/E_T$ for a peak $E_T = 0.78$ eV.

Photodetached electrons were extracted perpendicular to the laser and ion beams in a single-field space-focusing electron collection assembly and projected onto a time- and position-sensitive microchannel-plate-based detector.[41,43] The space focusing conditions were kept the same in all the measurements reported here with an extraction field of ∼14 V/cm. The measurement of both position and TOF for each electron allows the determination of the three-dimensional velocity distribution of the photoelectrons over the full 4π steradian solid angle. Since the electron velocity vector is measured, both the center-of-mass electron kinetic energy (eKE) and the laboratory-frame photoelectron angular distributions were simultaneously recorded. Defining the face of the electron detector as the $x-y$ plane, the *x*- and *y*-velocity components of the photoelectrons were determined from the detected position *and* TOF. The *z* velocity component is determined *only* from the TOF and is the limiting factor in the eKE resolution. Higher resolution *N*(eKE) spectra are found by selecting only electrons with minimal velocity components perpendicular to the face of the electron detector (v_z-sliced *N*(eKE) spectrum). The slicing parameter is typically chosen to allow not more than ∼10% of an individual velocity vector to be along the *z*-axis. The intensity distribution in a v_z-sliced spectrum is influenced by the width of the velocity slice. The original intensity distribution can be recovered in a sliced spectrum by taking into account the effective detector acceptance function (DAF) if the laser polarization is in the $x-y$ plane.[44] A resulting DAF-corrected, v_z-sliced photoelectron spectrum represents the probability distribution for measuring a photodetached electron with a particular kinetic energy, *P*(eKE). A series of calibration *P*(eKE) spectra of I^- and O^- were recorded using photon energies ranging from 1.71 to 4.82 eV in order to determine the instrumental resolution function over a broad range of photoelectron energies. The photoelectron energy resolution is observed to vary linearly in eKE with a fwhm of 0.023 eV at

eKE = 0 and 0.28 eV at eKE = 2.0 eV. Recording only photoelectrons that were detected in coincidence with one or more neutral particles arriving at the photofragment detector enhanced discrimination against laser-correlated background.

A PPC measurement allows discrimination between a photodetached electron correlated with a stable neutral cluster from one correlated with dissociated products. Separation of DPD events (1 electron + 2 momentum-matched fragments) from stable photodetachment events (1 electron + 1 neutral particle) is accomplished by counting the measured events. Due to the neutral particle detection efficiency (≈50%) and detector dead time, false coincidences contaminate the discrimination. Discrimination is improved by performing a "spherical gating" procedure on the measured single particle events, selecting as stable events only those that arrive at the center-of-mass of the parent ion beam. Photodetachment measurements on atomic I^- indicate that the optimal size for discrimination is a sphere of 1 mm radius, representing the projection of the interaction volume onto the photofragment detector face, as determined by the size of the interaction region, and the ion beam velocity and angular distributions. This procedure effectively removes those events correlated with a single neutral fragment resulting from a DPD event in which the second fragment was not detected. Inevitably as E_T approaches zero or the dissociation lifetime approaches the ion flight time from the interaction region to the detector (≈20 μs for the conditions of this experiment), discrimination between stable and dissociative events becomes impossible. In addition, as the mass difference between the products becomes large, the heavy fragment will recoil less and contribute more to the spherically gated spectrum. The neutral fragment detection efficiency is also a function of the beam velocity and therefore the mass of a product fragment; this does not affect the shape of the $N(E_T)$ spectra in the different systems but can influence the calculated branching ratios by reduced detection of coincident photofragments. The branching ratios reported here thus represent upper limits for the stable fraction.

Results

In these experiments, DPD from all anionic clusters was observed, yielding neutral iodine atoms and the associated solvent molecule. In addition to DPD, photodetachment yielding stable neutral clusters was observed. First, the photoelectron-photofragment correlation spectra acquired from 257 nm DPD of the solvated iodide clusters are presented. Photoelectron images and spectra follow, and are then resolved into distributions for either stable or dissociated neutral clusters. The I atom electronic-state-dependence of the DPD half-collision dynamics is examined using the $N(E_T)$ spectra corresponding to the ground and excited spin−orbit states of iodine. Finally, the energetics of stable and dissociative photodetachment in these cluster anions is discussed.

Photoelectron-Photofragment Coincidence Spectra: DPD Dynamics. The results of these experiments can be conveniently presented in a PPC spectrum of the photoelectron kinetic energy and the translational energy released into the DPD products, $N(E_T$,eKE). This spectrum reveals the partitioning of the available energy between photoelectrons and photofragment translational energy directly. Using the new imaging detector, the PPC spectrum has the P(eKE) distribution parallel to the vertical axis and the E_T distribution, $N(E_T)$, parallel to the horizontal axis. The corresponding one-dimensional spectra are obtained by integrating the two-dimensional coincidence spectrum over the complementary variable; the P(eKE) and v_z-sliced

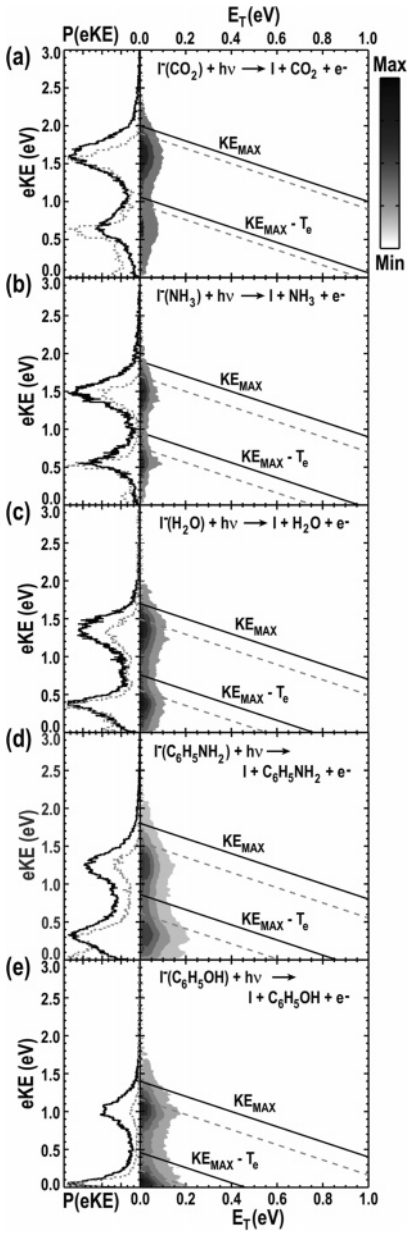

Figure 1. Photoelectron-photofragment coincidence spectra, $N(E_T$,-eKE), from 257 nm DPD of (a) $I^-(CO_2)$, (b) $I^-(NH_3)$, (c) $I^-(H_2O)$, (d) $I^-(C_6H_5NH_2)$, and (e) $I^-(C_6H_5OH)$. The photoelectron P(eKE) spectra (solid lines) and the v_z-sliced N(eKE) spectra (dashed lines) are shown along the vertical axes. The measured KE_{MAX} limits determined for the coincidence data using both the full P(eKE) spectrum and a v_z-sliced N(eKE) spectrum are shown as the solid and dashed lines, respectively.

N(eKE) spectra are shown as the projections along the vertical axes as the solid and dashed lines, respectively. DPD events are constrained by conservation of energy to lie within a triangle formed by the horizontal and vertical axes and the maximum available kinetic energy, KE_{MAX}. KE_{MAX} is determined from the 5% level on the PPC spectra representing the nominal false coincidence contour.

The PPC spectra acquired from DPD of $I^-(CO_2)$, $I^-(NH_3)$, $I^-(H_2O)$, $I^-(C_6H_5NH_2)$, and $I^-(C_6H_5OH)$ are presented in Figure 1a−e, respectively. The two-dimensional coincidence spectra themselves are generated using the full P(eKE) spectrum in concidence with the $N(E_T)$ spectra shown in Figure 5. The measured KE_{MAX} limits determined using both the full P(eKE) spectrum and a v_z-sliced N(eKE) spectrum at higher resolution are shown as the solid and dashed lines, respectively. Performing

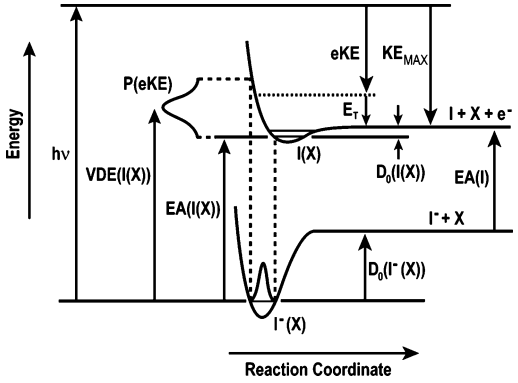

Figure 2. Schematic energy level diagram illustrating the relationship between the photon energy, $h\nu$, and the eKE and E_T distributions in the DPD of an anionic cluster. Quantities shown include the electron affinity of iodine, EA(I), the vertical detachment energy of the anionic cluster, VDE(I(X)), the adiabatic electron affinity of the neutral cluster, EA(I(X)), the kinetic energy released into the dissociating fragments, E_T, and the bond dissociation energies of the neutral cluster, $D_0(I(X))$, and the anionic cluster, $D_0(I^-(X))$.

the v_z-slicing procedure, as described above, enhances the resolution of the photoelectron kinetic energy spectrum, providing a more accurate value for KE_{MAX}. The v_z-sliced N(eKE) spectra also accentuate any signal near eKE = 0, as seen most clearly in the $I^-(C_6H_5NH_2)$ spectrum in Figure 1d that now shows a clear threshold photodetachment feature. The spectra show that the majority of the excess photon energy appears as eKE, with only a small fraction partitioned to the E_T release between the neutral fragments. Note that the two regions correlating $I(^2P_{3/2})$ and $I(^2P_{1/2})$ DPD with the neutral fragments are not equivalent within each of these spectra. The region associated with DPD from $I^-(CO_2)$ yielding $I(^2P_{3/2})$ (large eKE feature) extends to slightly larger E_T values than the region associated with DPD yielding $I(^2P_{1/2})$ (small eKE feature). An opposite, larger effect is observed with DPD of $I^-(C_6H_5NH_2)$ in Figure 1d. In this system a significantly larger E_T is seen for the $I(^2P_{1/2}) + C_6H_5NH_2$ products. These results show that the half-collision dynamics of these systems depend on the final spin−orbit state of the iodine atom. In contrast, the $N(E_T,eKE)$ spectra generated from DPD of $I^-(NH_3)$, $I^-(H_2O)$, and $I^-(C_6H_5OH)$ in Figure 1b,c,e, respectively, show equal partitioning of E_T for the two states, consistent with state-independent half-collision dynamics for the resulting neutral clusters.

The measurement of E_T and eKE in coincidence provides a direct measure of the bond dissociation energy of the anionic cluster, $D_0(I^-(X))$. A schematic energy level diagram of a general DPD process to a single electronic state of a neutral I(X) cluster is illustrated in Figure 2. The bond dissociation energy for the anionic cluster is given by

$$D_0(I^-(X)) = h\nu - EA(I) - KE_{MAX} \quad (1)$$

In this equation, $h\nu$ is the photon energy and EA(I) is the electron affinity of the iodine atom. If the potential energy surface of the neutral cluster has a minimum energy (bound) configuration similar in geometry to the bound anionic cluster, as illustrated in Figure 2, the neutral fragments produced in a DPD event are generated from the region of the Franck−Condon projection higher in energy than the asymptotically separated products. In this formula, no account has been taken for any internal energy remaining in the molecular fragments. The empirically determined KE_{MAX} for each of the clusters studied in this investigation, using the higher resolution v_z-sliced correlation spectra, are reported in Table 1. In fact, due to the poor eKE resolution and the relative low binding energies of these cluster anions, these values for KE_{MAX} yield values for the cluster dissociation energies 0.2−0.3 eV too low. The dissociation energies are discussed further in the section on DPD energetics below.

TABLE 1: Maximum Kinetic Energies, KE_{MAX}, for the Products of DPD[a]

DPD products	KE_{MAX}	DPD products	KE_{MAX}
$I + CO_2 + e^-$	1.90 ± 0.04	$I + C_6H_5NH_2 + e^-$	1.55 ± 0.04
$I + NH_3 + e^-$	1.70 ± 0.04	$I + C_6H_5OH + e^-$	1.20 ± 0.03
$I + H_2O + e^-$	1.60 ± 0.04		

[a] The values for KE_{MAX} (eV) are empirically determined from v_z-sliced correlation spectra and are shown as the dashed diagonal limits in Figure 1. The quoted errors are dominated by the eKE resolution.

Photoelectron Images and Spectra. The photoelectron images and associated P(eKE) spectra for photodetachment of the solvated iodide clusters are shown in Figure 3. The laser polarization was set parallel to the y-axis of the images. These images and spectra are all v_z-sliced and the spectra are DAF-corrected. These data include photodetached electrons correlated with *both* stable and dissociating neutral clusters. In nearly all of the photoelectron images it is evident that the photodetached electron density is maximum perpendicular to the laser electric vector. This indicates a $\sin^2\theta$ photoelectron angular distribution, consistent with photodetachment from atomic p, or p-like, orbitals on the iodide chromophore. Quantitative differences in the energy-dependent photoelectron angular distributions will be further discussed below.

In general, the photoelectron images and spectra consist of two features. The electron binding energies ($eBE = E_{h\nu} - eKE$) observed in all of the cluster spectra are greater than the electron affinity of atomic iodine, so the spectra are all shifted to higher eBE (lower eKE) relative to the I^- spectrum in Figure 3a. The features in the images and the peaks in the P(eKE) spectra originate from photodetachment of the solvated I^- chromophore producing the neutral in either the $I(^2P_{3/2})$ ground state (larger radii features) or the $I(^2P_{1/2})$ spin−orbit excited state (smaller radii features). In addition to these two features, the $I^-(C_6H_5NH_2)$ image shown in Figure 3e exhibits a high-intensity component in the center of the photoelectron distribution, corresponding to a peak near eKE = 0. This shows that, in addition to the two direct photodetachment processes observed in the other systems, another electron ejection process occurs in this cluster. This feature is not readily apparent in the P(eKE) spectrum; however, it is clearly seen as a resolved peak in the v_z-sliced N(eKE) spectrum shown as the y-axis projection in Figure 1d.

The vertical detachment energies (VDE's) for the anionic clusters for each resolved product electronic state are given by the eBE of the peaks in the P(eKE) spectra. The $VDE(I^-(X))$ is the energy needed to remove an electron from the anionic cluster with no change in geometry between the anion and resulting neutral, and thus represents an upper limit to the EA of the neutral cluster, assuming no internal excitation in the parent anions. The VDEs and electronic state separation energies, $^2P_{1/2} \leftarrow {}^2P_{3/2}$, resulting from photoelectrons correlated with *both* stable and dissociative neutral clusters are compiled in Table 2.

The anisotropic photoelectron angular distributions seen in the photoelectron images are quantitatively characterized in the electric dipole approximation by the energy-dependent anisotropy parameter, β(eKE). The anisotropy parameter is determined from the measured photoelectron energy and angular distributions by fitting to the functional form for electric dipole

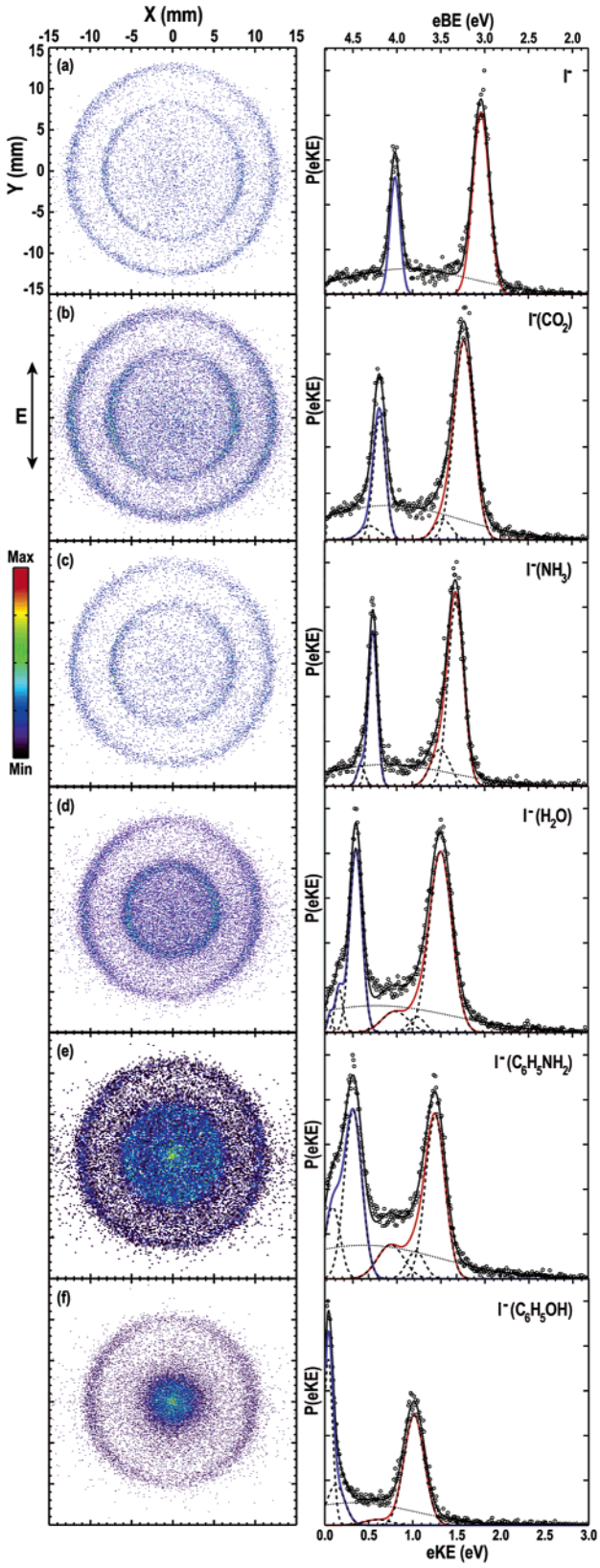

Figure 3. Photoelectron images and *P*(eKE) spectra from 257 nm photodetachment of (a) atomic I^-, (b) $I^-(CO_2)$, (c) $I^-(NH_3)$, (d) $I^-(H_2O)$, (e) $I^-(C_6H_5NH_2)$, and (f) $I^-(C_6H_5OH)$. Photoelectrons correlated with both stable and dissociating neutral fragments are included in both images and spectra. The laser polarization vector, **E**, is parallel to the *y*-axis in the images. In the *P*(eKE) spectra, experimental data points are represented by open circles, the solid fits correspond to the $I(^2P_{3/2})$ and $I(^2P_{1/2})$ channels and the broad dotted curves represent the background signal. The energy scales (eV) are eKE along the lower *x*-axes and eBE along the upper *x*-axes of each spectrum.

TABLE 2: Summary of Results from Photoelectron Spectra (Including *Both* Stable and Dissociative Products) for $I^-(X)$ Clusters at 257 nm [a]

anion	VDE	$^2P_{1/2} \leftarrow {}^2P_{3/2}$	$\beta(^2P_{3/2})$	$\beta(^2P_{1/2})$
I^-	3.06 ± 0.04	0.94	−0.54 ± 0.10	−0.73 ± 0.10
	3.059[b]	*0.943*[b]	*−0.58*[h]	*−0.80*[h]
$I^-(CO_2)$	3.24 ± 0.04	0.96	−0.65 ± 0.14	−0.73 ± 0.09
	3.224[c]	*0.955*[c]	*−0.69*[h]	*−0.72*[h]
$I^-(NH_3)$	3.33 ± 0.04	0.94	−0.69 ± 0.10	−0.63 ± 0.10
	3.319[d]	*0.94*[d]	*−0.71*[h]	*−0.65*[h]
$I^-(H_2O)$	3.50 ± 0.04	0.97	−0.79 ± 0.08	−0.26 ± 0.08
	3.449[e]	*0.963*[e]	*−0.77*[h]	*−0.46*[h]
$I^-(C_6H_5N\ H_2)$	3.57 ± 0.04	0.94	−0.57 ± 0.07	−0.09 ± 0.07
	3.62[f]		*−0.79*[h]	*−0.42*[h]
$I^-(C_6H_5O\ H)$	3.81 ± 0.04	0.98	−0.71 ± 0.14	−0.06 ± 0.08
	3.81[g]		*−0.80*[h]	*−0.02*[h]

[a] VDE is the vertical detachment energy, $^2P_{1/2} \leftarrow {}^2P_{3/2}$ is the spin−orbit state separation energy, $\beta(^2P_{3/2})$ and $\beta(^2P_{1/2})$ are the anisotropy parameters for ground- and excited-state photodetachment. Literature results for atomic I^- are included as well as previous measurements on the clusters studied here where available. The β(eKE) values in *italics* are values associated with photodetachment of atomic I^- at the same eKE as that observed from photodetachment of the cluster. All energies stated are in eV, and the energy uncertainty derives from the eKE resolution. [b] Reference 69. [c] Reference 15. [d] Reference 36. [e] Reference 35. [f] Calculated from heats of formation reported in ref 17. [g] Calculated from heats of formation reported in ref 13. [h] Reference 18.

transitions with linearly polarized light.[45,46]

$$P(\mathrm{eKE},\theta) = P(\mathrm{eKE})(1 + \beta(\mathrm{eKE})P_2(\cos\theta)) \qquad (2)$$

In this equation θ is the electron recoil angle relative to the laser electric field vector, **E**, and $P_2(\cos\theta) = {}^1/_2(3\cos^2\theta - 1)$, is the second-order Legendre polynomial in $\cos\theta$. $P(\mathrm{eKE},\theta)$ is the normalized doubly differential cross-section in eKE and θ and β(eKE) is the energy-dependent anisotropy parameter determined in the fit. In single-photon electric dipole transitions, β(eKE) is restricted to the range from −1 to +2, and for photodetachment from an atomic p orbital, as is the case for I^- in the energy domain studied here, β(eKE) will be less than or equal to 0.

Variations in β(eKE) for these clusters relative to atomic I^- result from both distortions of the filled 5p orbital of I^- in the different anionic clusters and the interaction of the continuum electron with the noncentral potential of the neutral complex. As a result of the energy dependence of β(eKE) above the detachment threshold,[45,46] a direct comparison of these distributions with atomic I^- at the same wavelength is not appropriate. Instead, they are compared with values for I^- at the same eKE above the detachment threshold obtained by Sanov and coworkers.[18] The results found by fitting eq 2 for β(eKE) in the present experiments are compared with I^- in Table 2. It is seen that in general the clusters have negative values of β(eKE) similar to atomic I^-, with the notable exceptions of the $I(^2P_{1/2})$ distributions for $I^-(H_2O)$ and $I^-(C_6H_5NH_2)$. In the case of $I^-(C_6H_5NH_2)$, the $I(^2P_{1/2})$ distribution is nearly isotropic, with $\beta(\mathrm{eKE}) > -0.10$, significantly different from I^-.

In addition to the energetic shifts and peak broadening observed in each of the *P*(eKE) spectra, variations in the peak intensities show that the spin−orbit state branching ratios vary for the different cluster spectra shown in Figure 3. Quantification of these differences is achieved by calculating the integrated electronic state channel branching ratios, $P(^2P_{1/2})/P(^2P_{3/2})$. Since the spectra for the different systems are broadened by internal excitation of the neutral clusters and an underlying laser-correlated background signal, each spectrum in Figure 3 was fit with a sum of five or six Gaussian curves, with the exception

TABLE 3: Spin-Orbit-State Branching Ratios, $P(^2P_{1/2})/P(^2P_{3/2})$, and Product Branching Ratios for Stable versus DPD and the Energetics Associated with Stable Photodetachment of $I^-(X)$ Clusters[a]

anion	$(P(^2P_{1/2})/P(^2P_{3/2}))_{TOTAL}$	$(P(^2P_{1/2})/P(^2P_{3/2}))_{STABLE}$	$(P(^2P_{1/2})/P(^2P_{3/2}))_{DPD}$	$P_{STABLE}/(P_{STABLE}+P_{DPD})$	VDE_{STABLE}
I^-		0.40 (*0.38*[b])			3.06 ± 0.04
$I^-(CO_2)$	0.41	0.42	0.41	0.18	3.22 ± 0.04
$I^-(NH_3)$	0.42	0.37	0.53	0.67	3.34 ± 0.04
$I^-(H_2O)$	0.56 (*0.63*[b])	0.56	0.60	0.63	3.48 ± 0.04
$I^-(C_6H_5NH_2)$	0.85	0.32	0.88	0.05	3.55 ± 0.04
$I^-(C_6H_5OH)$	0.73	0.24	0.82	0.09	3.77 ± 0.04

[a] The total branching ratio is calculated from data consisting of photoelectrons resulting from both stable and DPD events. The stable branching ratio is calculated from photoelectrons detected in coincidence with a single stable product, and the DPD ratio is calculated from photoelectrons detected in coincidence with two neutral, momentum-matched fragments. VDE_{STABLE} is the vertical detachment energy determined from the spherically gated *P*(eKE) corresponding to stable clusters. [b] Reference 18.

of I^-. In the case of I^-, *P*(eKE) was fit with three Gaussians; one for each of the peak features and a third to account for the background signal. This determined the shape of the background contribution used in the remaining fits. The broader *P*(eKE) spectra observed in the more strongly bound $I^-(H_2O)$, $I^-(C_6H_5NH_2)$, and $I^-(C_6H_5OH)$ clusters required six Gaussians for a better fit as seen in Figure 3. The branching ratios are determined from the fits for the two I product channels. The results obtained from this procedure applied to the total photoelectron spectra (photoelectrons correlated with *both* stable and dissociative neutral clusters), $(P(^2P_{1/2})/P(^2P_{3/2}))_{TOTAL}$, are listed in Table 3.

The *P*(eKE) spectra for DPD events only (excluding stable neutral complexes) compared to those for stable photodetachment events only, exhibit the same general features as those in Figure 3. Quantitative differences exist, however, as illustrated in the *P*(eKE) spectra resulting from either stable or dissociative photodetachment of $I^-(C_6H_5NH_2)$ and $I^-(C_6H_5OH)$, each presented separately in Figure 4. The column of spectra in Figure 4a result from photodetachment of $I^-(C_6H_5NH_2)$ and the column in Figure 4b are from $I^-(C_6H_5OH)$. The spectra in the top panels of each column are correlated with DPD, and the spectra in the middle panels are correlated with stable photodetachment only, generated by performing the spherical gating procedure on each $I^-(X)$ data set. The fitting procedure outlined above was used to quantify the spin−orbit branching ratios in the photoelectron spectra and to quantify the dissociative versus stable photodetachment yield for each system. The fraction of stable products reported in Table 3 is calculated from the measured number of events in the spherically gated photoelectron spectra of stable products compared to the triple coincidence events from a number of single data files for each system. The number of triple coincidence events is scaled by a factor of 2.4 to account for an assumed 50% detection efficiency for the second fragment and the ≈18% detector dead time loss for two-particle events in these experiments. It is likely that 50% represents an upper limit to the particle detection efficiency, as previously discussed, so these ratios should be interpreted as upper limits to the fraction of stable products, amplifying a point made at the end of Experiment concerning dissociation lifetime and fragment velocity effects. The comparisons of these fits for the two systems are shown in the bottom frames of Figure 4. The relative intensities of $I(^2P_{3/2})$ and $I(^2P_{1/2})$ vary in both spectra, showing that production of excited-state $I(^2P_{1/2})$ is associated with significantly fewer stable products, particularly in $I^-(C_6H_5NH_2)$. This same behavior was observed in the $I^-(NH_3)$ spectra when resolved for stable versus dissociative products; however this spectrum is not presented here.

Energetic shifts are also observed in the spectra resolved for stable and dissociative products. In the $I^-(C_6H_5OH)$ and $I^-(H_2O)$ spectra, shifts of 0.06 and 0.05 eV, respectively, are observed

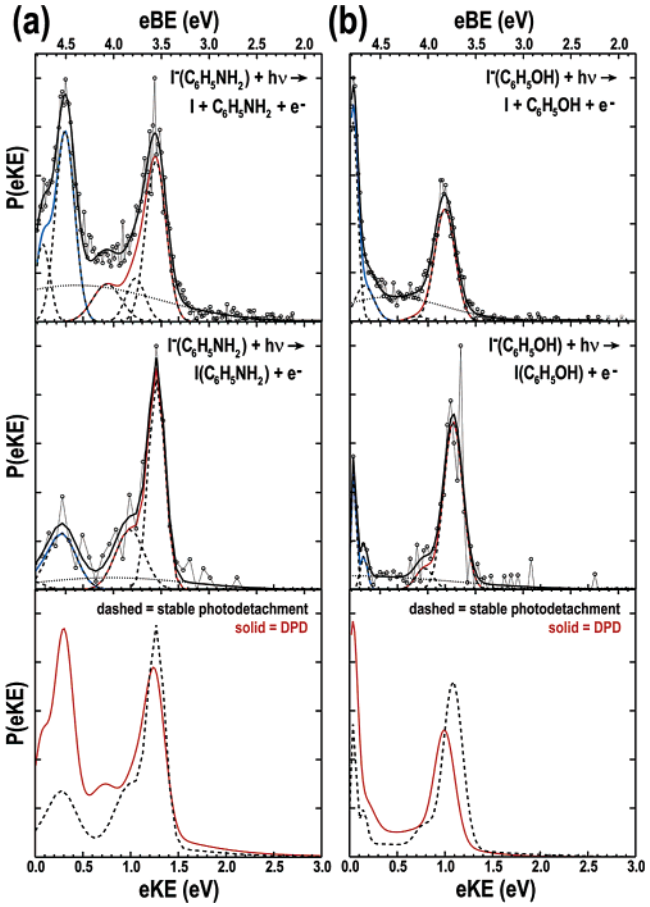

Figure 4. Photoelectron *P*(eKE) spectra comparing the photoelectron distributions correlated with DPD (top frames) with those correlated with stable photodetachment (middle frames) as discussed in the text. The spectra and fits in column a are for $I^-(C_6H_5NH_2)$, and those in column b are for $I^-(C_6H_5OH)$.

in the $I(^2P_{3/2})$ channel in the dissociative spectrum relative to the stable spectrum, consistent with production of stable clusters at the highest eKE's. A similar difference was observed upon comparing the spectra from $I^-(CO_2)$, $I^-(NH_3)$ and $I^-(C_6H_5NH_2)$, with a shift of 0.03 eV to lower eKE for $I(^2P_{3/2})$ DPD compared to $I(^2P_{3/2})$ photodetachment, yielding stable neutral clusters. The vertical detachment energies found in the *P*(eKE) spectra for stable neutral clusters, VDE_{STABLE}, and VDE_{DPD} for dissociative products are given in Tables 3 and 4, respectively. It is expected that higher resolution photoelectron measurements would reveal a more striking variation in these spectra.

The quantitative differences between the *P*(eKE) spectra for stable clusters compared to DPD events are seen in the spin−orbit-state branching ratios. The DPD branching ratios are compiled in Table 3 as $(P(^2P_{1/2})/P(^2P_{3/2}))_{DPD}$, and the stable

TABLE 4: Summary of the DPD Energetics for $I^-(X)$ Clusters[a]

neutral products	$\langle E_T(I(^2P_{3/2})+X)\rangle$	$\langle E_T(I(^2P_{1/2})+X)\rangle$	VDE_{DPD}	$D_0(I^-(X))$
$I + CO_2$	0.028 ± 0.003	0.025 ± 0.003	3.25 ± 0.04	0.16
	$1.1 \le eKE \le 2.2$	$0.0 \le eKE \le 1.0$		
$I + NH_3$	0.017 ± 0.002	0.020 ± 0.002	3.37 ± 0.04	0.29
	$0.95 \le eKE \le 2.0$	$0.0 \le eKE \le 0.95$		
$I + H_2O$	0.028 ± 0.003	0.026 ± 0.003	3.53 ± 0.04	0.44
	$0.85 \le eKE \le 2.0$	$0.0 \le eKE \le 0.85$		
$I + C_6H_5NH_2$	0.032 ± 0.003	0.050 ± 0.005	3.58 ± 0.04	0.50
	$0.65 \le eKE \le 1.9$	$0.0 \le eKE \le 0.65$		
$I + C_6H_5OH$	0.040 ± 0.004	0.044 ± 0.004	3.83 ± 0.03	0.73
	$0.45 \le eKE \le 1.6$	$0.0 \le eKE \le 0.45$		

[a] $\langle E_T(I(^2P_{3/2,1/2})+X)\rangle$ are the state-dependent average E_T over the eKE ranges indicated. VDE_{DPD} are determined from the P(eKE) spectra resulting from electrons correlated with dissociating neutral clusters only. The anionic bond dissociation energies, $D_0(I^-(X))$, are calculated using eq 3 and have the same errors as the VDE_{DPD}. All energies are in eV.

photodetachment branching ratios given as $(P(^2P_{1/2})/P(^2P_{3/2}))_{STABLE}$. The values found for DPD of $I^-(CO_2)$ and $I^-(H_2O)$ are, to within the error of the fitting procedure, the same as those ratios calculated when considering photoelectrons correlated with only stable events. Differences are seen in the spin−orbit branching ratios for $I^-(NH_3)$, $I^-(C_6H_5NH_2)$, and $I^-(C_6H_5OH)$, however. The largest effects are seen for $I^-(C_6H_5NH_2)$ and $I^-(C_6H_5OH)$, where the ratio varies from 0.32 and 0.24 for the stable channel to 0.88 and 0.82 for DPD, respectively.

In addition to spin−orbit branching ratios, the fraction of stable products can be measured. Using the same fitting routine outlined above on spherically gated photoelectron spectra, the percentage of neutral clusters that remain bound over the 16−22 μs flight time from the interaction region to the photofragment detector was determined for each system. The upper limits for these branching ratios are given in Table 3 as $P_{STABLE}/(P_{STABLE} + P_{DPD})$ and indicate that there is a large difference in the percentage of clusters that remain bound in the systems studied here, ranging from 5% for $I^-(C_6H_5NH_2)$ to 67% for $I^-(NH_3)$.

Photofragment Images and E_T Spectra. The results obtained from monitoring the neutral clusters that dissociate upon photodetachment are now presented. Figure 5 shows the neutral photofragment images and associated $N(E_T)$ spectra acquired from photodetachment of (a) atomic I^-, and DPD of (b) $I^-(CO_2)$, (c) $I^-(NH_3)$, (d) $I^-(H_2O)$, (e) $I^-(C_6H_5NH_2)$, and (f) $I^-(C_6H_5OH)$. The $N(E_T)$ spectra for the clusters in frames b−f are obtained from the coincidence data by integrating over eKE ranges correlated with the production of ground and spin−orbit excited I, as determined from the fits to the DPD P(eKE) spectra. The solid $N(E_T)$ spectra are correlated with $I(^2P_{3/2})$ fragments and the dashed spectra with $I(^2P_{1/2})$ fragments; the ranges of eKE for each of the spin−orbit states correlated with the spectra are listed in Table 4, along with the average $\langle E_T\rangle$ for each distribution. The neutral image correlated with atomic iodine consists of a sharp spot produced by the stable I atom, providing a measure of the size of the beam when projected onto the detector. This $N(E_T)$ spectrum peaks at 0.002 eV, with a fwhm of 0.003 eV when a product mass distribution of 63 and 64 amu is considered. This choice of masses gives the highest false $\langle E_T\rangle$. Additional product masses were considered to explore the effects; the resulting $N(E_T)$ spectra converged to zero as the chosen masses approached the known values of 127 and 0 amu. This shows that false coincidences with stable or long-lived neutral complexes in the cluster spectra do not significantly perturb the results.

The neutral images acquired for the clusters exhibit broader distributions due to the E_T release in DPD. The relative sizes of the images are affected by both the energy release and the mass difference between the two neutral fragments. For fragments with a large mass difference, such as $I + NH_3$ and $I + H_2O$ in Figure 5c,d, the iodine atom primarily remains localized along the parent beam and the lighter solvent molecule is ejected further out of the beam axis. Product masses that are nearly equal, such as $I + C_6H_5NH_2$ and $I + C_6H_5OH$ in Figure 5e,f, lead to ejection of both the atomic and molecular fragments significantly out of the parent beam axis. The $I + CO_2$ system in Figure 5b is kinematically between these two limits.

The photofragment images and $N(E_T)$ spectra shown in Figure 5 reveal that the fragments associated with $I(NH_3)$ dissociation receive less E_T than any of the other clusters studied here. The peak in the $N(E_T)$ spectrum is very close to zero; however, the spectrum extends to significantly higher E_T ($\approx$0.10 eV) than the false coincidence background spectrum recorded in the I^- experiment. This shows that $I(NH_3)$ is produced with low internal energies and is consistent with the branching ratio, indicating that 67% of the $I(NH_3)$ complexes remain bound after photodetachment of the anionic cluster. In contrast, the photofragment images acquired from the DPD of $I^-(C_6H_5OH)$ and $I^-(C_6H_5NH_2)$ are considerably broader, and the $N(E_T)$ spectra extend above $E_T \approx 0.20$ eV. No significant photofragment anisotropy was observed in the images and angular distributions, consistent with sequential DPD, in which photodetachment is followed by unimolecular decomposition of the nascent neutral.

As discussed for the $N(E_T$,eKE) spectra, subtle differences are observed between the $I(^2P_{3/2})$ and $I(^2P_{1/2})$ product channels for the DPD of $I^-(CO_2)$, with the $I(^2P_{3/2})$ $N(E_T)$ exhibiting a slightly larger E_T distribution. The $N(E_T)$ spectra for the two spin−orbit states of the I atom product have been normalized to unity to facilitate comparison between the two potential energy surfaces that the neutral clusters are formed on. This is shown quantitatively as the difference between average E_T for each product electronic state $\langle E_T(I(^2P_{3/2})+X)\rangle$ and $\langle E_T(I(^2P_{1/2})+X)\rangle$ tabulated in Table 4. Error bars have been included in the $I + CO_2$ $N(E_T)$ spectra at the $\langle E_T\rangle$ values for each of the electronic state distributions to indicate that the difference observed in the two spectra is outside of statistical fluctuations and results from state-dependent dissociation dynamics. A larger effect, but in the opposite electronic state of the I atom, is observed for the $I(^2P_{3/2})$ and $I(^2P_{1/2})$ product channels for the DPD of $I^-(C_6H_5NH_2)$. In this case, $\langle E_T(I(^2P_{1/2})+X)\rangle$ is 0.050 eV, while $\langle E_T(I(^2P_{3/2})+X)\rangle$ is only 0.032 eV. The $N(E_T)$ spectra resulting from DPD of $I^-(NH_3)$, $I^-(H_2O)$, and $I^-(C_6H_5OH)$ show no product-state dependence.

Dissociative Photodetachment Energetics. As discussed in the section on the $N(E_T$,eKE) spectra, the cluster anion bond dissociation energies calculated using eq 1 are significant underestimates of the stability of these anions as a result of the relatively low eKE resolution in this experiment. An alternative

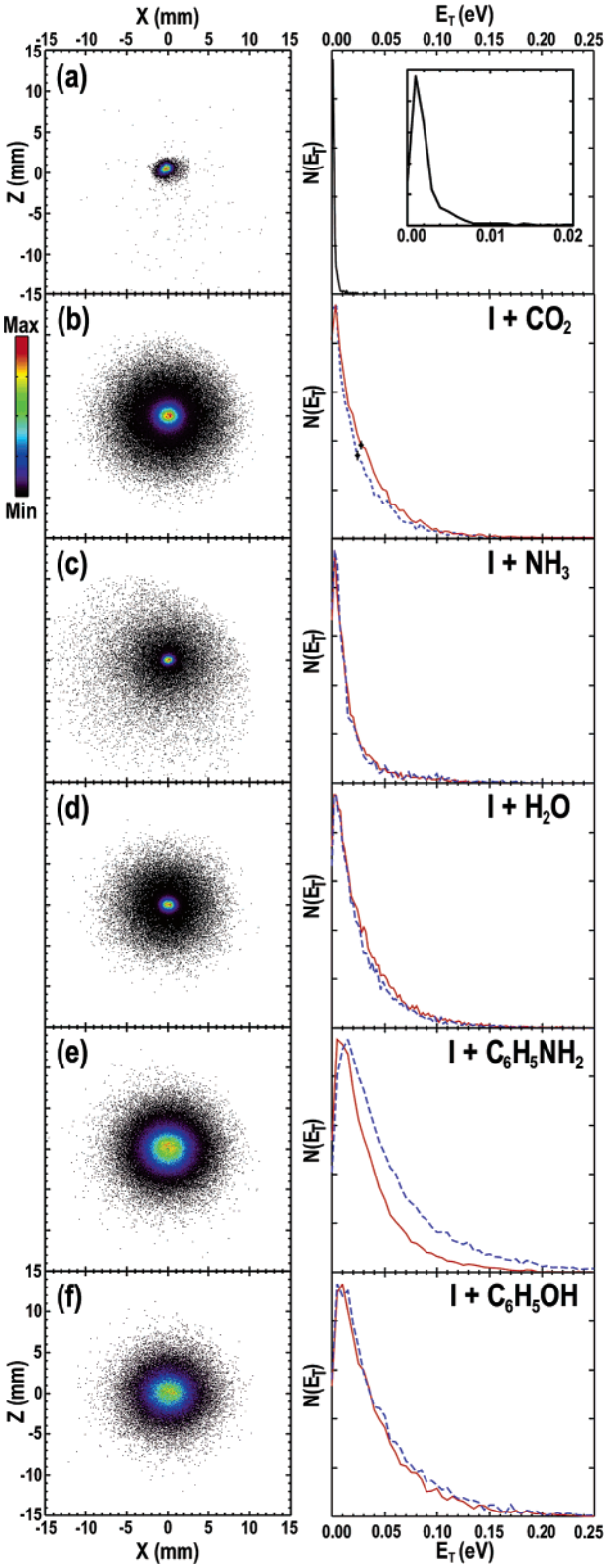

Figure 5. Neutral photofragment images and associated electronic-state-dependent $N(E_T)$ spectra for DPD of (a) atomic I^-, (b) $I^-(CO_2)$, (c) $I^-(NH_3)$, (d) $I^-(H_2O)$, (e) $I^-(C_6H_5NH_2)$, and (f) $I^-(C_6H_5OH)$. Each $N(E_T)$ distribution is normalized to unity at the peak. The $N(E_T)$ spectrum associated with photodetachment of atomic I^- is used to quantify the upper limit for two-body dissociation background signal and includes a magnified inset in a. The solid $N(E_T)$ spectra correspond to neutral fragments for DPD leading to the $I(^2P_{3/2})$ + X product channel, and the dashed spectra represent the $I(^2P_{1/2})$ + X product channel. Statistical (Poisson) error bars are shown in the $I^-(CO_2)$ spectrum in frame b at the $\langle E_T \rangle$ values for this system reported in Table 4.

approach to quantifying the $D_0(I^-(X))$ from the measurement is to use the VDE for ground-state DPD in conjunction with $\langle E_T \rangle$. The shift in the VDE relative to I^- is expected to primarily arise from stabilization of the cluster anion owing to the stronger attractive forces in the anion. Inclusion of $\langle E_T \rangle$ in the energy balance accounts for the fact that many of the neutrals are produced above the neutral cluster dissociation asymptote. This gives the approximate equation for the cluster anion bond dissociation energies:

$$D_0(I^-(X)) \approx \mathrm{VDE}_{\mathrm{DPD}}(I(X)) - \mathrm{EA}(I) - \langle E_T \rangle \qquad (3)$$

Using $\langle E_T \rangle$ to estimate the repulsion between the neutrals is clearly an approximation and assumes that all neutrals are produced with no internal excitation. In the present case where the repulsion on the neutral surface is not expected to be large this should be a reasonable assumption. The anionic bond dissociation energies determined using eq 3 are given in Table 4. These results are consistent with the previously reported values for the stability of the cluster anions reported in the Introduction, as a result of the low E_T for DPD in these systems. In the cases of $I^-(C_6H_5NH_2)$ and $I^-(C_6H_5OH)$, the results reported here are the first microscopic measurements of the stability of these anions, complementing the earlier bulk mass spectrometric measurements.

Discussion

The experiments presented here probe the interactions between I^- and several simple solvent molecules, and the even weaker interactions between the neutral constituents. These clusters all exhibit photoelectron spectra characteristic of photodetachment from a core I^- moiety, a result of the greater electron affinity of the iodine atom relative to any possible anionic states in the solvent molecules. This discussion initially addresses the state-dependent half-collision dynamics observed in the $N(E_T)$ spectra of $I^-(CO_2)$ and $I^-(C_6H_5NH_2)$. Then, the photodetachment dynamics are discussed, with particular emphasis on the variations observed in the spectra of $I^-(C_6H_5NH_2)$. Finally, potential complications arising from the chromophores $C_6H_5NH_2$ and C_6H_5OH are addressed.

State-Dependent Half-Collision Dynamics. When direct DPD occurs on a repulsive surface, the $N(E_T)$ spectrum is proportional to the projection of the vibrational wave function of the anion onto the multidimensional reaction coordinate along which dissociation proceeds. When there is Franck−Condon overlap with a repulsive region along the reaction coordinate, the topography of the potential surface dictates the width of the measured $N(E_T)$ spectrum, while the magnitude of E_T is proportional to the repulsive energy of the fragments in the equilibrium geometry of the anion. The situation becomes more complicated when the initial anion and the final neutral cluster have similar structures. In this case, DPD only occurs if the total energy on the neutral surface exceeds the binding interaction between the neutral constituents. This will lead to DPD occurring by a sequential mechanism, where the neutral undergoes unimolecular decomposition long after the electron has departed and a significant fraction of stable complexes are produced. The $N(E_T)$ distribution is expected to peak near $E_T = 0$, as seen in the present results shown in Figure 5. This is consistent with previous observations of structured ZEKE spectra for $I^-(CO_2)$ that are lifetime broadened into a continuum for large internal excitations.[19]

Variations in the $N(E_T)$ spectra for the $I(^2P_{3/2})$ and $I(^2P_{1/2})$ DPD channels are observed for $I^-(CO_2)$ and $I^-(C_6H_5NH_2)$.

While the interactions between the neutral products are multidimensional, to a first approximation, a one-dimensional reaction coordinate can be considered as in Figure 2. The observed variations in E_T arise in this approximation from different slopes in the Franck−Condon region for the $I(^2P_{3/2}) + X$ and $I(^2P_{1/2}) + X$ surfaces. These interactions, and thus the slopes of the potential energy surfaces, are dependent on the orientation of the atomic orbitals on iodine relative to the solvent molecule.[47] In a diatomic approximation, the solvent molecule can be assumed to be a spherical particle interacting with the $5p^5$ I atom. The atomic p-orbital aligned along the internuclear axis experiences a different interaction with the solvent molecule than either of the other two p-orbitals.[48] In $I(^2P_{3/2})$−rare-gas interactions, this results in splitting the ground electronic state of the open-shell neutral cluster into two states denoted $X(^2\Sigma_{1/2})$ and $I(^2\Pi_{3/2})$.[3,15]

In the case of the neutral $I(CO_2)$ cluster, high-resolution photoelectron spectra showed that the 0.028 eV splitting of the $I(^2P_{3/2})$ ground state of iodine into the $X(^2\Sigma_{1/2})$ and $I(^2\Pi_{3/2})$ states was observable, as in halogen−rare-gas atomic interactions.[19,49] The empirically determined structures of $I(CO_2)$ showed that the I−C bond length differs by 0.157 Å between the $X(^2\Sigma_{1/2})$ and $I(^2\Pi_{3/2})$ states, with the $X(^2\Sigma_{1/2})$ state having the shorter bond length.[19] The photoelectron energy resolution of the present experiments was not able to resolve these low-lying states; however, if they were resolved, an E_T dependence would be expected. Beyond the diatomic approximation, the shapes of the solvent molecules studied here lead to different interactions of all three atomic p-orbitals on the I atom with the solvent. Depending on which orbital the electron is removed from in the closed shell anion, different repulsive interactions may result, leading to final-state dependences as observed in the $N(E_T)$ spectra of $I + CO_2$ and $I + C_6H_5NH_2$.

As noted above, the state dependence in the $N(E_T)$ for $I + C_6H_5NH_2$ is larger and in the opposite direction from $I + CO_2$− the $I(^2P_{1/2})$ channel has a larger E_T in this system. The $I^-(C_6H_5NH_2)$ anion is significantly more strongly bound, by both ion−dipole, hydrogen-bonding, and ion-induced-dipole interactions, due to the presence of the polarizable aromatic ring in aniline. In addition to affecting the $N(E_T)$ spectra, the photoelectron spectrum for this system exhibits considerably broader peaks resulting from distortion of the aniline in the cluster yielding greater internal excitation in the nascent neutral. Also, as noted in the product branching ratios in Table 3, photodetachment of $I^-(C_6H_5NH_2)$ yields few stable $I(C_6H_5NH_2)$, particularly in the excited state, consistent with Franck−Condon overlap with a more repulsive region in the excited state of the neutral cluster.

Stable/Dissociative Product Branching Ratios. The fraction of stable products observed in these experiments ranges from nearly 0.7 for $I(NH_3)$ and $I(H_2O)$ down to less than 0.1 for $I(C_6H_5OH)$ and $I(C_6H_5NH_2)$. As discussed previously, these represent upper limits to the fraction of stable complexes as a result of the flight time relative to the predissociation lifetime, $N(E_T)$ distributions, kinematics, and detection efficiency assumptions. It would be interesting to compare these results to theoretical predictions taking into account the Franck−Condon projection of the anionic wave function onto the neutral surface, followed by unimolecular decomposition of the energized neutral complex. This is beyond the scope of the present study. Given that the ion flight times from the interaction region to the detector only vary from 17.3 μs ($I(NH_3)$) to 21.4 μs ($I(C_6H_5OH)$), it is unlikely that lifetime effects bias the comparison of the different systems. The predissociation lifetimes of vibrationally excited neutral clusters have been reported for many weakly bound systems.[26,27,50−53] The range of lifetimes for vibrationally excited states prior to dissociation span time scales from picoseconds when large internal excitations are present to tens of nanoseconds for clusters with small internal excitations, although the predissociation lifetime of the $(HCN)_2$ was found to be 1.7 μs.[54] Future studies at a number of different beam energies could provide further insights into lifetime effects on these branching ratios; however, at the present time we will just take the fraction of stable products observed as an upper limit.

Photodetachment Dynamics. In I^- photodetachment, the electronic state branching ratio $P(^2P_{1/2})/P(^2P_{3/2})$ has been observed to deviate from the statistical value of 0.5.[18] This results from variations in the energy-dependent photodetachment cross-sections for the two final electronic states. Given that photodetachment from an atomic p-orbital yields outgoing s- and d-waves, the s-wave partial cross-section is expected to decrease less rapidly as the eKE approaches zero at threshold.[55,56] Since the present measurements are all at 257 nm, and the clusters have different electron affinities, variations in the spin−orbit state branching ratios as a function of the available energy are not a surprise. This effect is in addition to solvent-dependent changes in the electronic structure of these anion clusters. The most important effect seen in the product branching ratios is the significant change in the $P(^2P_{1/2})/P(^2P_{3/2})$ ratio for stable and dissociative product channels for $I^-(NH_3)$, $I^-(C_6H_5NH_2)$, and $I^-(C_6H_5OH)$ clusters. It is found in these systems that the stable channel favors ground-state $I(^2P_{3/2}) + X$ products significantly. This implies that the ground-state $I(^2P_{3/2})$−X clusters that remain stable have better Franck−Condon overlap with the parent anions, as mentioned above in the case of $I^-(C_6H_5NH_2)$.

The photoelectron energy and angular distributions indicate that photodetachment from these clusters involves ejection of an electron from an atomic p-like orbital on the iodide chromophore. The angular distributions are the most sensitive probe of the high-lying orbitals of the anion cluster, and in fact we find that the β(eKE) values measured for $I^-(CO_2)$, $I^-(NH_3)$, the $I(^2P_{3/2})$ state of $I^-(H_2O)$, and both states of $I^-(C_6H_5OH)$ are not appreciably different from those observed in the photodetachment of I^-.[18] However, as shown by the β(eKE) values in Table 2, substantial variations in the photoelectron angular distributions were observed in both detachment channels of $I^-(C_6H_5NH_2)$, and in the $I(^2P_{1/2})$ channel of $I^-(H_2O)$. In these systems and for these electronic states the photoelectron angular distribution is significantly more isotropic than in I^-. This indicates suppression of the d-wave ($l = 2$) angular momentum component in the photodetached electron, the presence of another electron detachment mechanism, or both. The common feature in the systems that show significant differences is the permanent dipole in the solvent molecule and the potentially enhanced dipole of the neutral cluster when configured in the equilibrium geometry of the anionic cluster, although phenol does not exhibit a significant perturbation.

To explore the effect of the dipole field of the nascent neutral clusters on the photodetached electrons, density functional theory calculations were performed using the Gaussian 03 program suite to predict the dipole moments of the neutral clusters configured in the optimized geometries of the anionic clusters.[57] Geometry optimizations of each of the anionic clusters were performed at the B3LYP level with the aug-cc-pvdz basis set for the solvent molecules and the DGDZVP basis set for the iodide atom. Subsequently, the dipole moment of each neutral

cluster was calculated with the cluster constituents frozen in the geometrical configurations of the optimized anionic clusters. These calculations give $\mu = 0.38$ D for $I{\cdot}CO_2$, 1.46 D for $I{\cdot}NH_3$, 2.35 D for $I{\cdot}H_2O$, 5.30 D for $I{\cdot}C_6H_5NH_2$, and 4.43 D for $I{\cdot}C_6H_5OH$. The largest dipole moments are found for those solvent molecules containing polarizable aromatic rings, with that of the $I{\cdot}C_6H_5NH_2$ cluster significantly greater than any of the other systems. A significant interaction between the transient dipole of the neutral cluster configured in the anion geometry and the continuum photoelectron is therefore expected for this system that could result in the observed relatively isotropic angular distribution and be responsible for the threshold detachment feature observed in Figures 1d and 3e.

A potential mechanism for production of the threshold detachment feature in aniline involves capture of a fraction of the incipient continuum electrons by the large dipole field of the neutral cluster configured in the anionic geometry.[58] The diffuse dipole-bound electron would not bind the neutral constituents, so in the subsequent dissociation a low-energy free electron could be liberated. There must be a charge-transfer-to-solvent aspect to this process; however, as an excited $(I{\cdot}C_6H_5NH_2)^{*-}$ anion might dissociate above threshold to yield $I^- + C_6H_5NH_2$, $I + C_6H_5NH_2^-$, and $I + C_6H_5NH_2 + e^-$. No evidence for production of I^- during the 1.8 ps laser pulse by photodetachment of I^- by a second photon was observed; however, this does not fully rule out occurrence of this channel, due to the short laser pulse. Since the electron is initially localized on I^-, it is expected that absorption of a photon yields a state with the electron transferred to the solvent. The second product channel in this mechanism involves the anilide anion; however, this species is not stable in either valence[59] or dipole-bound states. The dipole moment in isolated aniline is only $\mu_{C_6H_5NH_2} = 1.13$ D,[38] considerably less than needed to bind an electron. Any charge-transfer-to-solvent in this system, then, will be expected to exhibit a low-energy threshold detachment feature consistent with a two-step process involving photoexcitation of an excited state of the cluster anion followed by dissociation and autodetachment from anilide.

Previous studies have shown that the interaction between the incipient continuum electron and the dipole of the resulting neutral cluster or the solvent itself may have a significant impact on the photodetachment dynamics. In the $I^-(H_2O)$ system the interaction between the permanent dipole and the excess electron is sufficient to support a transient charge-transfer-to-solvent dipole-bound anionic excited state.[58] Isolated H_2O has a large dipole moment ($\mu_{H_2O} = 1.854$ D) that is enhanced in the geometry of the $I^-(H_2O)$ anionic cluster as shown by the calculations carried out in this study and in ref 18. However, no autodetachment signal is observed in the $I^-(H_2O)$ cluster. Autodetachment has been previously observed in $(OCS)_2^-$ and attributed to excited states of covalently bound isomers of this homomolecular dimer anion.[60,61] Bonding in the $I^-(C_6H_5NH_2)$ cluster is noncovalent so a different mechanism for threshold detachment in this system must be operative, such as that proposed in the previous paragraph. Given the similarities of the interactions in $I^-(H_2O)$ and $I^-(C_6H_5NH_2)$, however, the question is why no threshold detachment is observed in $I^-(H_2O)$. The fundamental difference between the two is that aniline is a large, polarizable object, so even though the permanent dipole is smaller, it has a greater tendency to capture the incipient continuum electrons. In addition, aniline has significantly more low-lying electronic states than water that can be involved in the formation of temporary anionic states.[59]

The decreased anisotropy in the angular distributions observed in both channels for the photodetachment of $I^-(C_6H_5NH_2)$ was also observed in studies of the 267 nm photodetachment of $I^-(CH_3CN)$.[18] Of the clusters investigated in the present study, $I^-(CH_3CN)$ most closely resembles $I^-(C_6H_5NH_2)$ with the inclusion of a C−N bond. However, the bonding in acetonitrile is significantly different, with an electron-rich C−N triple bond instead of the more diffuse lone pairs on the N atom in aniline. In addition, the large permanent dipole in CH_3CN ($\mu = 3.924$ D)[38] supports a long-lived dipole-bound state, facilitating photodissociation to yield $I + CH_3CN^-$ below and possibly above the photodetachment threshold.[62,63] Photodestruction of $I^-(CH_3CN)$ above threshold could lead to competition between direct DPD, photodissociation to $I^- + CH_3CN$, and photodissociation to I + internally excited CH_3CN^- that could subsequently autodetach to yield low-energy electrons. However, no autodetachment signal was observed for $I^-(CH_3CN)$ in ref 18, as the dipole moment of the CH_3CN fragment is evidently strong enough to retain any captured electrons. In the case of $I^-(C_6H_5NH_2)$, the calculations presented here indicate that while the dipole moment of the $C_6H_5NH_2$ fragment is enhanced in the geometry of the anionic cluster, the dipole moment of isolated $C_6H_5NH_2$ cannot support a stable, dipole-bound $C_6H_5NH_2^-$ after cluster dissociation. Thus, relaxation of a transient $C_6H_5NH_2^-$ after dissociation will yield a low-energy autodetached electron.

In the state-dependent $N(E_T)$ spectra in the DPD of $I^-(C_6H_5NH_2)$, it is interesting to note that the channel with the larger E_T is the $I(^2P_{1/2}) + C_6H_5NH_2$ product channel and that this channel also has a nearly isotropic photoelectron angular distribution, indicating either s-wave ($l = 0$) photodetachment or an indirect electron emission mechanism at threshold. At the larger eKEs in this channel, photodetachment is undoubtedly direct, and given that the angular momentum carried away by the photoelectron and the electronic angular momenta of the products are less in this channel, it is possible that the half-collision dynamics in this case lead to higher E_T as a result of angular momentum conservation. The clusters under study here are produced in a jet-cooled environment, with rotational temperatures expected to be on the order of 35 K;[64] thus the parent rotational angular momentum is limited. The half-collisions probed in these experiments have impact parameters constrained by the initial geometry of the anion. The relative spatial orientation of the atomic and molecular orbitals of the cluster constituents will also govern the electronic interactions in the anion and neutral. It is interesting to speculate that a stereo-electronic coupling of the cluster anion structure to the photodetachment continuum leads to the different product channels, with different angular momentum constraints leading to the differences observed in the $N(E_T)$ spectra for the $I(^2P_{1/2}) + C_6H_5NH_2$ and $I(^2P_{3/2}) + C_6H_5NH_2$ dissociation channels.

Finally, we note that the interaction of I^- with both aniline and phenol is considerably stronger than their nonaromatic homologues. The alcoholic H atom in phenol is relatively acidic, and thus the potential for proton-transfer reactions yielding $HI - C_6H_5O^-$ complexes must be considered. It has been shown that when the chloride anion interacts with phenol, proton transfer occurs.[65] The electron affinity (EA) of the phenoxyl radical is 2.25 eV,[66] and we have found the VDE ≈ EA for the $I(C_6H_5OH)$ cluster to be 3.81 eV. If the proton-transfer reaction were to occur, the phenoxide anion would be stabilized compared to the free anion, but not by 1.4 eV. In addition, the similarity of the $I^-(C_6H_5OH)$ photoelectron spectra to perturbed I^- strongly argues against the occurrence of proton transfer in

the complex. Aniline is less acidic than phenol, so the likelihood of proton transfer is even less in that case. The similarity of the observed photoelectron spectra in these iodide−aromatic complexes also argues against any significant absorption by either phenol or aniline playing a role in the photodetachment process. It is important to keep in mind, however, that both of these molecules readily absorb ultraviolet radiation[67,68] and have the potential to act as a chromophore in the cluster. At this photon energy, it is possible that excitation of the aromatic molecules in the $I^-(C_6H_5NH_2)$ and $I^-(C_6H_5OH)$ clusters to their S_1 states occurs, but there is no evidence this is affecting the photodetachment process under study here. Studies of the wavelength dependence of the photodetachment dynamics of these clusters will provide further insights into this question.

Summary

An experimental study of the stable and dissociative photodetachment of the solvated iodide clusters $I^-(CO_2)$, $I^-(NH_3)$, $I^-(H_2O)$, $I^-(C_6H_5NH_2)$, and $I^-(C_6H_5OH)$ at 257 nm has been presented. Photoelectron-photofragment coincidence spectroscopy was used to investigate the half-collision dynamics of the nascent neutral clusters produced in the equilibrium geometries of the anionic precursors. The photoelectron angular distributions for the $I(^2P_{3/2})$ and $I(^2P_{1/2})$ product channels were measured and compared to I^-, revealing the effect of clustering on the photodetachment dynamics. The largest effects were seen in the ion−dipole systems $I^-(C_6H_5NH_2)$ and $I^-(H_2O)$. These coincidence measurements allowed investigation of the spin−orbit-state dependence of the DPD dynamics. Spin−orbit branching ratios, $P(^2P_{1/2})/P(^2P_{3/2})$, were measured for stable and dissociative neutral products, and the fraction of stable products are also reported. The translational energy distributions were found to peak near $E_T = 0$, with small average energy releases that were cluster-dependent. A dependence of the dissociation dynamics on the I spin−orbit state was found in both the $I(CO_2)$ and $I(C_6H_5NH_2)$ clusters, showing that the potential energy surfaces governing dissociation into $I(^2P_{1/2}) + X$ and $I(^2P_{3/2}) + X$ products are not equivalent for these clusters when produced in the equilibrium structure of the anion by photodetachment. In addition to the spin−orbit-state-dependent dissociation dynamics in the DPD of $I^-(C_6H_5NH_2)$, a threshold photodetachment process was observed for this system. These observations indicate that additional studies on $I^-(C_6H_5NH_2)$ at other wavelengths would be fruitful for understanding the photodetachment dynamics of this cluster.

Acknowledgment. This research was supported by the National Science Foundation (Grant CHE-0136195). M.B. is pleased to acknowledge support for his stay at UCSD from the Joint Research Center of the European Commission under the Sixth Framework Program's Marie Curie Transfer of Knowledge fellowship (Contract No. MTKD-CT-2004-509761). We are grateful to Morton A. Fineman for discussions.

References and Notes

(1) Castleman, A. W.; Bowen, K. H. *J. Phys. Chem.* **1996**, *100*, 12911.

(2) Sanov, A.; Lineberger, W. C. *Phys. Chem. Chem. Phys.* **2004**, *6*, 2018.

(3) Zhao, Y.; Yourshaw, I.; Reiser, G.; Arnold, C. C.; Neumark, D. M. *J. Chem. Phys.* **1994**, *101*, 6538.

(4) Arnold, D. W.; Bradforth, S. E.; Kim, E. H.; Neumark, D. M. *J. Chem. Phys.* **1995**, *102*, 3510.

(5) Arnold, D. W.; Bradforth, S. E.; Kim, E. H.; Neumark, D. M. *J. Chem. Phys.* **1995**, *102*, 3493.

(6) Gomez, H.; Taylor, T. R.; Neumark, D. M. *J. Chem. Phys.* **2002**, *116*, 6111.

(7) Loh, Z. M.; Wilson, R. L.; Wild, D. A.; Bieske, E. J.; Zehnacker, A. *J. Chem. Phys.* **2003**, *119*, 9559.

(8) Osterwalder, A.; Nee, M. J.; Zhou, J.; Neumark, D. M. *J. Chem. Phys.* **2004**, *121*, 6317.

(9) Mabbs, R.; Pichugin, K.; Surber, E.; Sanov, A. *J. Chem. Phys.* **2004**, *121*, 265.

(10) Markovich, G.; Pollack, S.; Giniger, R.; Cheshnovsky, O. *J. Chem. Phys.* **1994**, *101*, 9344.

(11) Dang, L. X.; Garrett, B. C. *J. Chem. Phys.* **1993**, *99*, 2972.

(12) Kebarle, P. *Annu. Rev. Phys. Chem.* **1977**, *28*, 445.

(13) Paul, G. J. C.; Kebarle, P. *Can. J. of Chem.* **1990**, *68*, 2070.

(14) Paul, G. J. C.; Kebarle, P. *J. Am. Chem. Soc.* **1991**, *113*, 1148.

(15) Arnold, D. W.; Bradforth, S. E.; Kim, E. H.; Neumark, D. M. *J. Chem. Phys.* **1992**, *97*, 9468.

(16) Bassmann, C.; Boesl, U.; Yang, D.; Drechsler, G.; Schlag, E. W. *Int. J. Mass Spectrom. Ion Processes* **1996**, *159*, 153.

(17) Caldwell, G. W.; Masucci, J. A.; Ikonomou, M. G. *Org. Mass Spectrom.* **1989**, *24*, 8.

(18) Mabbs, R.; Surber, E.; Sanov, A. *J. Chem. Phys.* **2005**, *122*, 0543081.

(19) Zhao, Y.; Arnold, C. C.; Neumark, D. M. *J. Chem. Soc., Faraday Trans.* **1993**, *89*, 1449.

(20) Brumbaugh, D. V.; Kenny, J. E.; Levy, D. H. *J. Chem. Phys.* **1983**, *78*, 3415.

(21) Stephenson, T. A.; Rice, S. A. *J. Chem. Phys.* **1984**, *81*, 1083.

(22) Jacobson, B. A.; Humphrey, S.; Rice, S. A. *J. Chem. Phys.* **1988**, *89*, 5624.

(23) Nimlos, M. R.; Young, M. A.; Bernstein, E. R.; Kelley, D. F. *J. Chem. Phys.* **1989**, *91*, 5268.

(24) Becucci, M.; Lakin, N. M.; Pietraperzia, G.; Castelluci, E.; Brechignac, P.; Coutant, B.; Hermine, P. *J. Chem. Phys.* **1999**, *110*, 9961.

(25) Becucci, M.; Pietraperzia, G.; Castellucci, E.; Brechignac, P. *Chem. Phys. Lett.* **2004**, *390*, 29.

(26) Satink, R. G.; Bakker, J. M.; Meijer, G.; Helden, G. v. *Chem. Phys. Lett.* **2002**, *359*, 163.

(27) Oudejans, L.; Miller, R. E. *Annu. Rev. Phys. Chem.* **2001**, *52*, 607.

(28) Yoder, L. M.; Barker, J. R. *Phys. Chem. Chem. Phys.* **2000**, *2*, 813.

(29) Yoder, L. M.; Barker, J. R. *J. Phys. Chem. A* **2000**, *104*, 10184.

(30) Vernon, M. F.; Lisy, J. M.; Kwok, H. S.; Krajnovich, D. J.; Tramer, A.; Shen, Y. R.; Lee, Y. T. *J. Phys. Chem.* **1981**, *85*, 3327.

(31) Johnson, R. D.; Burdenski, S.; Hoffbauer, M. A.; Giese, C. F.; Gentry, W. R. *J. Chem. Phys.* **1986**, *84*, 2624.

(32) Bomse, D. S.; Cross, J. B.; Valentini, J. J. *J. Chem. Phys.* **1983**, *78*, 7175.

(33) Yoder, L. M.; Barker, J. R.; Lorenz, K. T.; Chandler, D. W. *Chem. Phys. Lett.* **1999**, *302*, 602.

(34) Parsons, B. F.; Chandler, D. W. *J. Phys. Chem. A* **2003**, *107*, 10544.

(35) Markovich, G.; Giniger, R.; Levin, M.; Cheshnovsky, O. *J. Chem. Phys.* **1991**, *95*, 9416.

(36) Frischkorn, C.; Zanni, M. T.; Davis, A. V.; Neumark, D. M. *Faraday Discuss.* **2000**, *115*, 49.

(37) Evans, D. H.; Keesee, R. G.; Castleman, A. W. J. *J. Chem. Phys.* **1987**, *86*, 2927.

(38) Landolt-Bornstein *Numerical Data and Functional Relationships in Science and Technology*; Springer-Verlag: Heidelberg, Germany, 1982; Vol. Group 2, Vol. 14, Subvolume a.

(39) Sherwood, C. R.; Hanold, K. A.; Garner, M. C.; Strong, K. M.; Continetti, R. E. *J. Chem. Phys.* **1996**, *105*, 10803.

(40) Continetti, R. E. *Int. Rev. Phys. Chem.* **1998**, *17*, 227.

(41) Davies, J. A.; LeClaire, J. E.; Continetti, R. E.; Hayden, C. C. *J. Chem. Phys.* **1999**, *111*, 1.

(42) Continetti, R. E.; Cyr, D. R.; Neumark, D. M. *Rev. Sci. Instrum.* **1992**, *63*, 1840.

(43) Alconcel, L. S.; Deyerl, H. J.; DeClue, M.; Continetti, R. E. *J. Am. Chem. Soc.* **2001**, *123*, 3125.

(44) Bowen, M. S.; Continetti, R. E. *J. Phys. Chem. A* **2004**, *108*, 7827.

(45) Cooper, J.; Zare, R. N. *J. Chem. Phys.* **1968**, *48*, 942.

(46) Zare, R. N. *Mol. Photochem.* **1972**, *4*, 1.

(47) Aquilanti, V.; Liuti, G.; Pirani, F.; Vecchiocattivi, F. *J. Chem. Soc., Faraday Trans.* **1989**, *2*, 955.

(48) Haberland, H. *Z. Phys. A* **1982**, *307*, 35.

(49) Sanov, A.; Faeder, J.; Parson, R.; Lineberger, W. C. *Chem. Phys. Lett.* **1999**, *313*, 812.

(50) Huang, Z. S.; Jucks, K. W.; Miller, R. E. *J. Chem. Phys.* **1986**, *85*, 3338.
(51) Jucks, K. W.; Miller, R. E. *J. Chem. Phys.* **1987**, *86*, 6637.
(52) Zhao, M.; Rice, S. A. *J. Chem. Phys.* **1992**, *96*, 7483.
(53) Lovejoy, C. M.; Schuder, M. D.; Nesbitt, D. J. *J. Chem. Phys.* **1986**, *85*, 4890.
(54) Kerstel, E. R. T.; Lehmann, K. K.; Gambogi, J. E.; Yang, X.; Scoles, G. *J. Chem. Phys.* **1993**, *99*, 8559.
(55) Wigner, E. P. *Phys. Rev.* **1948**, *73*, 1002.
(56) Farley, J. W. *Phys. Rev. A* **1989**, *40*, 6286.
(57) Frisch, M. J.; Trucks, G. W.; Schlegel, H. B.; Scuseria, G. E.; Robb, M. A.; Cheeseman, J. R.; J. A. Montgomery, J.; Vreven, T.; Kudin, K. N.; Burant, J. C.; Millam, J. M.; Iyengar, S. S.; Tomasi, J.; Barone, V.; Mennucci, B.; Cossi, M.; Scalmani, G.; Rega, N.; Petersson, G. A.; Nakatsuji, H.; Hada, M.; Ehara, M.; Toyota, K.; Fukuda, R.; Hasegawa, J.; Ishida, M.; Nakajima, T.; Honda, Y.; Kitao, O.; Nakai, H.; Klene, M.; Li, X.; Knox, J. E.; Hratchian, H. P.; Cross, J. B.; Adamo, C.; Jaramillo, J.; Gomperts, R.; Stratmann, R. E.; Yazyev, O.; Austin, A. J.; Cammi, R.; Pomelli, C.; Ochterski, J. W.; Ayala, P. Y.; Morokuma, K.; Voth, G. A.; Salvador, P.; Dannenberg, J. J.; Zakrzewski, V. G.; Dapprich, S.; Daniels, A. D.; Strain, M. C.; Farkas, O.; Malick, D. K.; Rabuck, A. D.; Raghavachari, K.; Foresman, J. B.; Ortiz, J. V.; Cui, Q.; Baboul, A. G.; Clifford, S.; Cioslowski, J.; Stefanov, B. B.; Liu, G.; Liashenko, A.; Piskorz, P.; Komaromi, I.; Martin, R. L.; Fox, D. J.; Keith, T.; Al-Laham, M. A.; Peng, C. Y.; Nanayakkara, A.; Challacombe, M.; Gill, P. M. W.; Johnson, B.; Chen, W.; Wong, M. W.; Gonzalez, C.; Pople, J. A. *Gaussian03*, Revision C.02, Gaussian Inc.: Wallingford, CT, 2004.
(58) Serxner, D.; Dessent, C. E. H.; Johnson, M. A. *J. Chem. Phys.* **1996**, *105*, 7231.
(59) Jordan, K. D.; Michejda, J. A.; Burrow, P. D. *J. Am. Chem. Soc.* **1976**, *98*, 7189.
(60) Surber, E.; Sanov, A. *Phys. Rev. Lett.* **2003**, *90*, 0930011.
(61) Surber, E.; Sanov, A. *J. Chem. Phys.* **2003**, *118*, 9192.
(62) Dessent, C. E. H.; Bailey, C. G.; Johnson, M. A. *J. Chem. Phys.* **1995**, *102*, 2006.
(63) Bailey, C. G.; Dessent, C. E. H.; Johnson, M. A. *J. Chem. Phys.* **1996**, *104*, 6976.
(64) Continetti, R. E.; Cyr, D. R.; Metz, R. B.; Neumark, D. M. *Chem. Phys. Lett.* **1991**, *182*, 406.
(65) DeTuri, V. F.; Ervin, K. M. *Int. J. Mass Spectrom. Ion Processes* **1998**, *175*, 123.
(66) Gunion, R. F.; Gilles, M. K.; Polak, M. L.; Lineberger, W. C. *Int. J. Mass Spectrom. Ion Processes* **1992**, *117*, 601.
(67) Etzkorn, T.; Klotz, B.; Sorensen, S.; Patroescu, I. V.; Barnes, I.; Becker, K. H.; Platt, U. *Atmos. Environ.* **1999**, *33*, 525.
(68) Sinclair, W. E.; Pratt, D. W. *J. Chem. Phys.* **1996**, *105*, 7942.
(69) Hanstorp, D.; Gustafsson, M. *J. Phys. B* **1992**, *25*, 1773.